Delft University of Technology

Platform for nodal topological superconductors in monolayer molybdenum dichalcogenides

Wang, Lin; Rosdahl, Tomas Orn; Sticlet, Doru

Important note
To cite this publication, please use the final published version (if applicable).
Please check the document version above.

Platform for nodal topological superconductors in monolayer molybdenum dichalcogenides

Lin Wang,[1,*] Tomas Orn Rosdahl,[1] and Doru Sticlet[1,2]

[1]*Kavli Institute of Nanoscience, Delft University of Technology, P.O. Box 4056, 2600 GA Delft, The Netherlands*
[2]*National Institute for Research and Development of Isotopic and Molecular Technologies, 67-103 Donat, 400293 Cluj-Napoca, Romania*

We propose a platform to realize nodal topological superconductors in a superconducting monolayer of MoX_2 (X = S, Se, Te) using an in-plane magnetic field. The bulk nodal points appear where the spin splitting due to spin-orbit coupling vanishes near the $\pm K$ valleys of the Brillouin zone and are six or twelve per valley in total. In the nodal topological superconducting phase, the nodal points are connected by flat bands of zero-energy Andreev edge states. These flat bands, which are protected by chiral symmetry, are present for all lattice-termination boundaries except zigzag.

I. INTRODUCTION

Fully gapped topological superconductors (TSCs), characterized by a global topological invariant in the Brillouin zone, have been the subject of intense investigation in recent years. They provide a platform for the creation of the Majorana quasiparticle [1–3], which has promising applications in quantum information [4–6]. Nodal superconductors, i.e., superconductors with nodal points or lines at the Fermi surface where the bulk gap vanishes, can also display nontrivial topological properties, becoming nodal TSCs [7–9]. Their topological invariants are only defined locally in the Brillouin zone, giving rise to flat bands or arcs of surface states in the nontrivial phase [10–12].

Intrinsic nodal TSCs are predicted to exist in unconventional superconductors, such as high-temperature d-wave superconductors [13], the heavy fermion systems [14–16], noncentrosymmetric superconductors [17,18], and Weyl superconductors [19]. However, intrinsic unconventional pairing is complex and ambiguous, and is furthermore not robust to disorder, making intrinsic nodal TSCs challenging experimentally. It is therefore desirable to engineer nodal TSCs using simpler components [20–22], such as conventional s-wave spin-singlet superconductors, similar to efforts in realizing fully gapped TSCs using proximity-induced s-wave pairing [23,24].

Two-dimensional monolayers of transition metal dichalcogenides (TMDs) [25] offer an opportunity to engineer nodal TSCs. Recent experiments show that several monolayer TMDs, such as MoS_2, $MoSe_2$, $MoTe_2$, WS_2, and $NbSe_2$, become superconducting [26–34], with a critical temperature, e.g., as large as 10 K observed in MoS_2 [28]. These superconductors possess an extremely high critical in-plane magnetic field, several times larger than the Pauli limit, due to a special type of Ising spin-orbit coupling (SOC) [28,30,35,36]. The Ising SOC results from the heavy atoms and the absence of inversion symmetry and acts as an effective Zeeman term

perpendicular to the TMD plane, with opposite orientation at opposite momenta, pinning electron spins to the out-of-plane direction [37,38]. Previous work predicts that hole-doped monolayer $NbSe_2$ with s-wave superconductivity near $\boldsymbol{\Gamma}$ becomes a nodal TSC in an in-plane magnetic field [39]. In their proposal, the bulk nodal points appear along Γ-M lines where the Ising SOC vanishes because of the in-plane mirror symmetry $M_x : x \rightarrow -x$. However, the potential of TMD materials such as MoS_2, $MoSe_2$, $MoTe_2$, and WS_2, which are superconducting at electron doping near the $\boldsymbol{K}$ valleys, to become nodal TSC is currently not known. Note that M_x does not guarantee the vanishing of SOC near the $\boldsymbol{K}$ valleys.

In this paper, we show that s-wave superconducting monolayers of molybdenum dichalcogenides (MoX_2, X = S, Se, Te) become nodal TSCs in the presence of an in-plane magnetic field. In this previously unknown topological phase, the bulk nodal points appear near the $\boldsymbol{K}$ valleys at special momenta where the SOC splitting vanishes. We find two regimes in the nodal topological phase, with six or twelve nodal points appearing near each valley, respectively. In the nodal topological phase, nodal points are connected by zero-energy Andreev flat band edge states, which are protected by a chiral symmetry originating from mirror symmetry in the MoX_2 plane and present for all edges except zigzag. Finally, we discuss possible experimental verification of the nodal topological phase.

II. MODEL

A monolayer MX_2 (MoS_2, $MoSe_2$, $MoTe_2$, or WS_2) consists of a triangular lattice of M atoms sandwiched between two layers of X atoms, each also forming a triangular lattice. The top and bottom X atoms project onto the same position in the layer of M atoms, such that when viewed from above, the monolayer has the hexagonal lattice structure shown in Fig. 1(a), with primitive lattice vectors $\boldsymbol{a}_1$ and $\boldsymbol{a}_2$. In the normal state, the monolayer MX_2 has a direct band gap at the $\pm K$ points. Near the ηK ($\eta = \pm$) points, the point group is C_{3h}, and the effective Hamiltonian of the lowest conduction
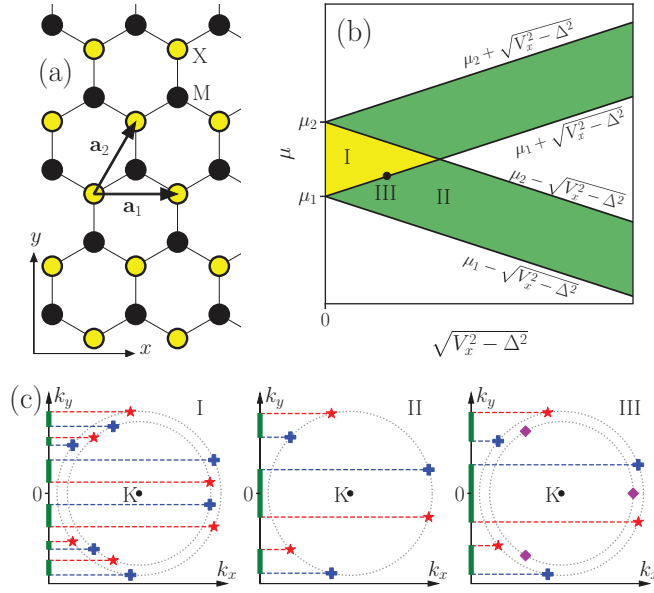
*Corresponding author: L.Wang-6@tudelft.nl

FIG. 1. (a) Top view of monolayer MX_2 lattice structure with primitive lattice vectors $\boldsymbol{a}_1$ and $\boldsymbol{a}_2$. (b) Phase diagram of the gap-closing condition as a function of μ and $\sqrt{V_x^2 - \Delta^2}$. Nodal points appear in regions where the gap closes, colored yellow (regime I) and green (regime II), with the phase boundaries given by $\mu = \mu_{1,2} \pm \sqrt{V_x^2 - \Delta^2}$. III represents the boundary between regimes I and II. (c) Sketch of nodal points near $\boldsymbol{K}$ valley. The chirality of nodal points with $+(\star)$ is $1(-1)$, and diamond denotes two overlapping nodal points of opposite chirality. Nodal point projections on the k_y axis determine topologically nontrivial phases with nonzero winding number (solid green lines).

band up to the third order in momentum $\boldsymbol{k} = (k_x, k_y)$ is

$$H_e^\eta(\boldsymbol{k}) = \frac{k^2}{2m^*} + \left[\lambda\eta + A_1 k^2 \eta + A_2\left(k_x^3 - 3k_x k_y^2\right)\right]\sigma_z \quad (1)$$

in the basis $[c_{\eta\boldsymbol{k}\uparrow}, c_{\eta\boldsymbol{k}\downarrow}]$, with $c_{\eta\boldsymbol{k}s}$ the annihilation operator for an electron in valley η at momentum $\boldsymbol{k}$ with spin $s = \uparrow, \downarrow$. We obtain this effective Hamiltonian from the $\boldsymbol{k} \cdot \boldsymbol{p}$ Hamiltonian near the $\pm\boldsymbol{K}$ valleys in Ref. [46] by the Löwdin partition method [47,48]. Here, the x (y) axis points along the zigzag (armchair) direction as in Fig. 1(a), m^* denotes the effective mass, λ and $A_{1,2}$ are SOC strengths, and $\sigma_{x,y,z}$ are the Pauli matrices in spin space. Material parameters are provided as Supplemental Material [49].

Including superconductivity with s-wave pairing and an in-plane magnetic field, the Bogoliubov-de Gennes (BdG) Hamiltonian in the basis $[c_{\eta\boldsymbol{k}\uparrow}, c_{\eta\boldsymbol{k}\downarrow}, c_{-\eta-\boldsymbol{k}\uparrow}^\dagger, c_{-\eta-\boldsymbol{k}\downarrow}^\dagger]$ is

$$H_{\mathrm{BdG}}^\eta(\boldsymbol{k}) = \left(\frac{k^2}{2m^*} - \mu\right)\tau_z + \left[\lambda\eta + A_1 k^2 \eta + A_2\left(k_x^3\right.\right.$$
$$\left.\left. - 3k_x k_y^2\right)\right]\sigma_z + V_x \sigma_x \tau_z + V_y \sigma_y + \Delta\sigma_y \tau_y, \quad (2)$$

where μ, $\tau_{x,y,z}$, Δ, and $V_{x,y}$ are the chemical potential, Pauli matrices in particle-hole space, the superconducting gap, and the Zeeman energy terms due to the magnetic field, respectively.

The BdG Hamiltonian $H_{\mathrm{BdG}}^\eta(\boldsymbol{k})$ has a particle-hole symmetry (PHS) $\mathcal{P}H_{\mathrm{BdG}}^\eta(\boldsymbol{k})\mathcal{P}^{-1} = -H_{\mathrm{BdG}}^{-\eta}(-\boldsymbol{k})$ where $\mathcal{P} = \tau_x \mathcal{K}$,

with $\mathcal{K}$ being the complex conjugation operator. Although time-reversal symmetry (TRS) $\mathcal{T} = i\sigma_y \mathcal{K}$ is broken by the magnetic field, $H_{\mathrm{BdG}}^\eta(\boldsymbol{k})$ respects an effective TRS $\tilde{\mathcal{T}}H_{\mathrm{BdG}}^\eta(\boldsymbol{k})\tilde{\mathcal{T}}^{-1} = H_{\mathrm{BdG}}^{-\eta}(-\boldsymbol{k})$ where $\tilde{\mathcal{T}} = M_{xy}\mathcal{T}$, with $M_{xy} = -i\sigma_z \tau_z$ the mirror symmetry in the monolayer plane. Therefore, $H_{\mathrm{BdG}}^\eta(\boldsymbol{k})$ has the chiral symmetry $\mathcal{C}H_{\mathrm{BdG}}^\eta(\boldsymbol{k})\mathcal{C}^{-1} = -H_{\mathrm{BdG}}^\eta(\boldsymbol{k})$ with $\mathcal{C} = \mathcal{P}\tilde{\mathcal{T}} = \sigma_x \tau_y$. As a result, $H_{\mathrm{BdG}}^\eta(\boldsymbol{k})$ is in class BDI, which is trivial in two dimensions for gapped systems [50,51] but can be nontrivial for nodal systems. We reduce the dimension to one by fixing two orthogonal directions $\boldsymbol{k}_\parallel$ and $\boldsymbol{k}_\perp$ in momentum space and considering each $H_{\mathrm{BdG}}^\eta(\boldsymbol{k}_\perp, \boldsymbol{k}_\parallel)$ at a fixed $\boldsymbol{k}_\parallel$ separately [11]. Although $\mathcal{P}$ and $\tilde{\mathcal{T}}$ are in general not symmetries of the one-dimensional (1D) Hamiltonian $H_{\mathrm{BdG}}^\eta(\boldsymbol{k}_\perp, \boldsymbol{k}_\parallel)$ at a fixed $\boldsymbol{k}_\parallel$ [52], because they flip the sign of both $\boldsymbol{k}_\parallel$ and $\boldsymbol{k}_\perp$ [53]; $\mathcal{C}$ is a symmetry for any choice of $\boldsymbol{k}_\parallel$. Therefore the 1D Hamiltonians $H_{\mathrm{BdG}}^\eta(\boldsymbol{k}_\perp, \boldsymbol{k}_\parallel)$ at a fixed $\boldsymbol{k}_\parallel$ belong to class AIII [54] and are thus characterized by an integer topological invariant: the winding number [50].

III. BULK NODAL POINTS

We begin investigating the topological phases of $H_{\mathrm{BdG}}^\eta(\boldsymbol{k})$ by finding the gap-closing conditions, which determine the bulk nodal points. Due to chiral symmetry, $H_{\mathrm{BdG}}^\eta(\boldsymbol{k})$ can be brought to a block off-diagonal form [11,55], with the upper off-diagonal element

$$A_\eta(\boldsymbol{k}) = -\left(\frac{k^2}{2m^*} - \mu\right) + \left[\lambda\eta + A_1 k^2 \eta + A_2\left(k_x^3 - 3k_x k_y^2\right)\right]\sigma_z$$
$$- V_x \sigma_x + V_y \sigma_y + i\Delta\sigma_z. \quad (3)$$

The gap-closing condition $\det[A_\eta(\boldsymbol{k})] = 0$ gives rise to two requirements:

$$\lambda\eta + A_1 k^2 \eta + A_2\left(k_x^3 - 3k_x k_y^2\right) = 0, \quad (4\mathrm{a})$$

$$\mu \pm \sqrt{V_x^2 + V_y^2 - \Delta^2} = \frac{k^2}{2m^*}. \quad (4\mathrm{b})$$

The first is the vanishing of spin splitting due to SOC [see Eq. (1)], and the second is the magnetic field closing the bulk gap at the Fermi circle without SOC. These two conditions arise because closing the gap with the magnetic field brings together bands that are coupled by SOC. The bands thus repulse, except at points in momentum space where the SOC vanishes and the gap closes. Such points manifest as crossings between the spin-split conduction bands in the normal-state dispersion, which are present near $\pm\boldsymbol{K}$ valleys in monolayer MoX_2 (X = S, Se, Te) but not WS_2, due to the relative strengths of SOC contributions from the d orbitals on the transition metal atoms and the p orbitals on the chalcogen atoms [56–58]. Therefore, the requirement (4a) is not met in WS_2, and we focus on MoX_2 in the following. The gap-closing requirements (4) are independent of the in-plane magnetic field orientation, so we set $V_y = 0$ in the following. Solving Eq. (4a) limits k to $k_{c1} \leqslant k \leqslant k_{c2}$ with $k_{c1,c2} = k_0 \pm k_0^2/(2A_0)$, $k_0 = \sqrt{-\lambda/A_1}$, and $A_0 = A_1/A_2$ [49]. Figure 1(b) shows a phase diagram of the gap-closing conditions as a function of μ and $\sqrt{V_x^2 - \Delta^2}$. The four phase boundaries $\mu = \mu_{1,2} \pm \sqrt{V_x^2 - \Delta^2}$ with $\mu_{1,2} = k_{c1,c2}^2/(2m^*)$ divide the diagram into regimes, with nodal points and therefore possible nontrivial phases in the colored regions (I and II).

IV. TOPOLOGICAL PHASES

In the gapless regimes of the phase diagram, Fig. 1(c) sketches the nodal points near the K valley along with their chirality $w(\boldsymbol{k}^i)$. The chirality of the nodal point at $\boldsymbol{k}^i = (k_\perp^i, k_\parallel^i)$ is the winding number around it and is ± 1 [11,18,55]. The nodal point chirality relates to the winding number W of the 1D Hamiltonian at a fixed $k_\parallel$ through $W(k_\parallel) = \sum_{k_\parallel^i < k_\parallel} w(\boldsymbol{k}^i)$, which means that we can obtain $W(k_\parallel)$ by counting the nodal point projections onto the $k_\parallel$ axis and keeping track of their chirality. For the zigzag direction $\boldsymbol{k}_\parallel = k_x \hat{\boldsymbol{x}}$, the nodal point projections cancel exactly, because the nodal points come in pairs with opposite chirality at each k_x and hence $W(k_x) = 0$ always. For any other direction, the nodal points do not cancel, and nontrivial phases thus exist for all directions $\boldsymbol{k}_\parallel$ other than zigzag. We show the projections of the nodal points on the armchair direction $\boldsymbol{k}_\parallel = k_y \hat{\boldsymbol{y}}$ and the corresponding segments of the k_y axis where $W(k_y) \neq 0$ (solid green lines). In regime I, there are two momentum circles (4b) near the K valley, with six nodal points each for a total of twelve. The nodal points divide the k_y axis into thirteen segments, with six segments topologically nontrivial. In regime II, there is only one momentum circle with six nodal points, such that the k_y axis separates into seven parts, with three nontrivial. At the boundary between regimes I and II (marked as III in the figure), pairs of nodal points of opposite chirality overlap on one momentum circle, such that only the other circle contributes to the winding number W, similar to regime II. The nodal points near the $-K$ valley are symmetric to the ones near K in k_x [see also Fig. 4(a)]. The preceding analysis applies equally to all three MoX$_2$ monolayers. In the following, we explore further details of the topological phases, focusing on nodal point projections on the armchair direction. Although we show examples for specific materials, we have verified that the physics is qualitatively the same for all three [49].

To complement the analysis of nodal point projections, Figs. 2(a) and 2(b) show computed phase diagrams of the winding number as a function of k_y and $\sqrt{V_x^2 - \Delta^2}$ at two chemical potentials, $\mu_1 < \mu < (\mu_1 + \mu_2)/2$ in (a) and $\mu < \mu_1$ in (b), respectively, representative of regimes I and II of Fig. 1. The phase diagrams are even in k_y, and the winding number is ± 2 due to equal contributions from the $\pm K$ valleys. The phase boundaries in Fig. 1(b) determine the range of the nontrivial regions in $\sqrt{V_x^2 - \Delta^2}$, while the maximum extent along k_y is bounded from above by $|k_y| \leqslant k_0$, independent of μ and $\sqrt{V_x^2 - \Delta^2}$ [49]. Sweeping over $\sqrt{V_x^2 - \Delta^2}$ in (a), the phase diagram transitions from regime I to II indicated by the vertical dashed line, such that the number of topologically nontrivial segments along k_y changes from six to three (also counting $-k_y$). In contrast, (b) is exclusively in regime II.

V. EXCITATION GAP AND EDGE STATES

Topologically nontrivial phases are protected by the topological excitation gap, which we define as $E_{\text{gap}}(\boldsymbol{k}_\parallel) = \min_{n, \boldsymbol{k}_\perp} |E_n(\boldsymbol{k}_\parallel, \boldsymbol{k}_\perp)|$, where $E_n(\boldsymbol{k})$ is the spectrum of $H_{\text{BdG}}^\eta(\boldsymbol{k})$, with n a band index. Figures 2(c) and 2(d) show maps of the topological excitation gap corresponding to the phase diagrams (a) and (b), respectively. In the nontrivial
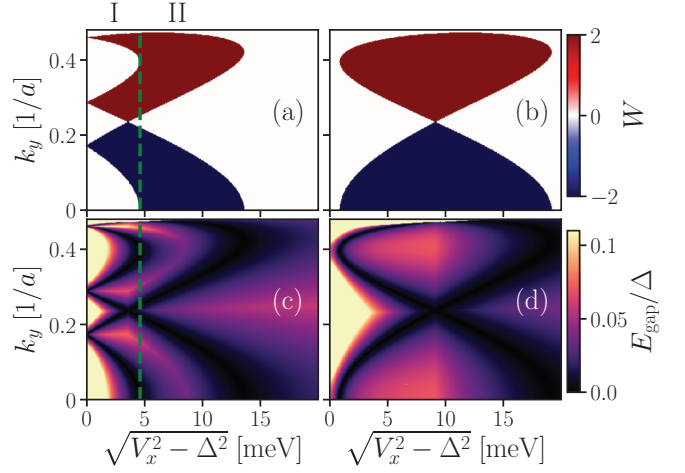

FIG. 2. Topological phase diagrams for the armchair direction $\boldsymbol{k}_\parallel = k_y \hat{\boldsymbol{y}}$ of monolayer MoSe$_2$. The winding number as a function of k_y and $\sqrt{V_x^2 - \Delta^2}$ with (a) $\mu_1 < \mu < (\mu_1 + \mu_2)/2$ and (b) $\mu < \mu_1$, in regimes I and II of Fig. 1. The phase diagrams for $(\mu_1 + \mu_2)/2 < \mu < \mu_2$ and $\mu > \mu_2$ are similar to (a) and (b), respectively, but with opposite winding numbers. (c), (d) The corresponding topological excitation gap E_{gap} to (a) and (b) separately. Data is obtained using the continuum model (2), and a is the lattice constant of the MX$_2$ lattice.

phase, we see that $E_{\text{gap}} \lesssim 0.1\Delta$ for MoSe$_2$ and similarly find $E_{\text{gap}} \lesssim 0.04\Delta$ for MoS$_2$ and $E_{\text{gap}} \lesssim 0.2\Delta$ for MoTe$_2$ [49]. Here, we emphasize that Δ may represent intrinsic superconductivity, which means that no proximity effect is required, and interface effects that tend to reduce the gap further are thus absent.

In a topologically nontrivial phase, edge states manifest at a monolayer lattice termination boundary. We investigate the edge states at an armchair edge by calculating the local density of states at the boundary, $\rho(E, x_B, k_y) = -\frac{1}{\pi} \text{Tr}[\text{Im} G(E, x_B, k_y)]$, with E the energy, x_B the coordinate of the armchair edge, and G the surface Green's function [59]. Figure 3(a) shows the local density of states obtained using parameters from regime I of Fig. 1(b), i.e., with 12 nodal points per valley. At zero energy, there are six sections of Andreev flat bands connecting nodal points, which exactly match the topologically nontrivial phases with nonzero winding number, marked by the vertical dotted lines, and the shaded regions in Fig. 3(b). In Fig. 3(b), we also present the decay length of the topologically nontrivial edge states and see that it is of the order 1 μm here.

VI. ARBITRARY EDGE DIRECTIONS

Although we have so far focused on an armchair edge, topologically nontrivial regimes exist for all lattice termination edges except zigzag. Using tight-binding models to simulate the MX$_2$ lattice [Fig. 1(a)] with Kwant [60], we characterize a lattice termination edge with a superlattice vector $\boldsymbol{T}$ at the angle ϕ relative to the armchair direction [49]. To investigate topological phases, we deform the hexagonal first Brillouin zone into the rectangle spanned by primitive reciprocal vectors $\hat{\boldsymbol{k}}_\parallel$ and $\hat{\boldsymbol{k}}_\perp$, which are parallel and,
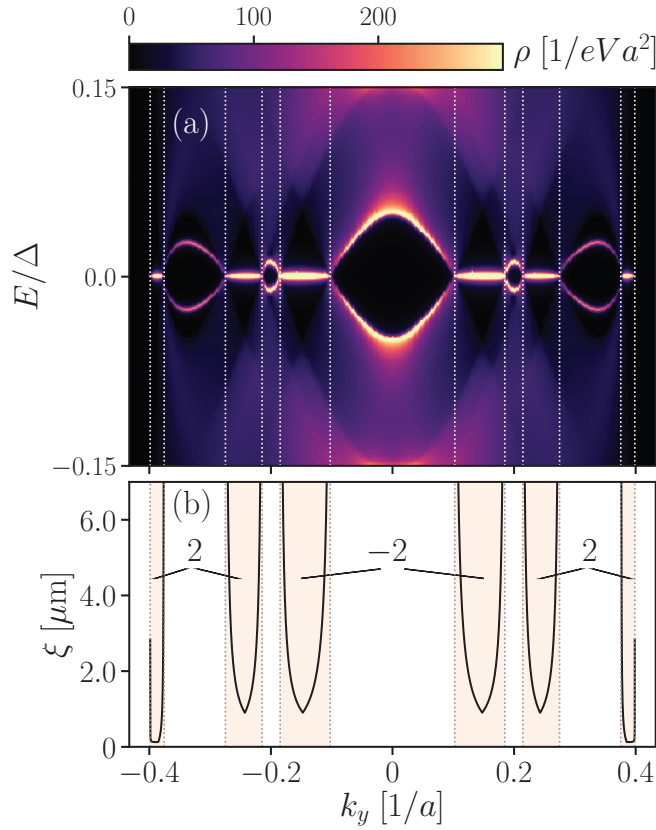
FIG. 3. (a) Density of states at the armchair edge as a function of k_y for monolayer MoS$_2$, with parameters in regime I of Fig. 1(b). Flat bands of zero-energy Andreev edge states where the winding number is nonzero between nodal point projections. (b) Decay length of the edge states in the topologically nontrivial phase. The nontrivial phases are marked by the shaded regions with the nonzero winding numbers in the insets. Data is obtained using an 11-orbital tight-binding model with $\mu = 1.8337$ eV, $\sqrt{V_x^2 - \Delta^2} = 1.5$ meV, and $\Delta = 0.8$ meV, see Supplemental Material.

FIG. 4. (a) Schematic of the hexagonal first Brillouin zone of the monolayer lattice, with nodal points around the high symmetric points $\pm \boldsymbol{K}$. For arbitrary edge cuts, we deform the Brillouin zone into a rectangle, illustrated by the dash-dotted lines and the $k_\parallel$ and $k_\perp$ axes, and project the nodal points onto $k_\parallel$. Flat bands of Andreev bound states exist for $k_\parallel$ where the winding number is nonzero (bold colored lines). For a generic edge cut, each nodal point generally projects onto a distinct $k_\parallel$, such that the winding number may take various values, e.g., ± 1 (green) or ± 2 (purple) in the sketch. (b) Phase diagram of the winding number for an edge with $\phi \approx 1.2°$. The phase diagram is rich with the winding number ± 1, ± 2, ± 3, or ± 4. Data is obtained from an 11-orbital tight-binding model for MoS$_2$ with $\mu = 1.8390$ eV and $\Delta = 0.8$ meV, see Supplemental Material.

respectively, transverse to $\boldsymbol{T}$ [61], and project the nodal points onto the $k_\parallel$ axis [Fig. 4(a)]. As before, flat bands exist in segments of the $k_\parallel$ axis where the winding number is nonzero. Unlike an armchair edge, the nodal points near $\pm \boldsymbol{K}$ generally do not project pairwise onto the same $k_\parallel$ at a generic boundary, and the winding number can take other values than ± 2, e.g., ± 1 (green lines). Figure 4(b) is an example of a phase diagram for an edge direction with $\phi \approx 1.2°$ and shows that the winding number can be ± 1, ± 3, and even ± 4. For generic lattice terminations other than armchair, nodal topological phases are thus not only present but also manifest in rich phase diagrams with large winding numbers.

VII. SUMMARY AND DISCUSSION

We have shown that a superconducting monolayer MoX$_2$ (X = S, Se, Te) can become a nodal TSC in the presence of an in-plane magnetic field. The bulk nodal points occur at special momenta near $\pm \boldsymbol{K}$ valleys in the Brillouin zone where the spin splitting due to SOC vanishes and can be 6 or 12 in each valley. For all lattice termination edges except zigzag, the 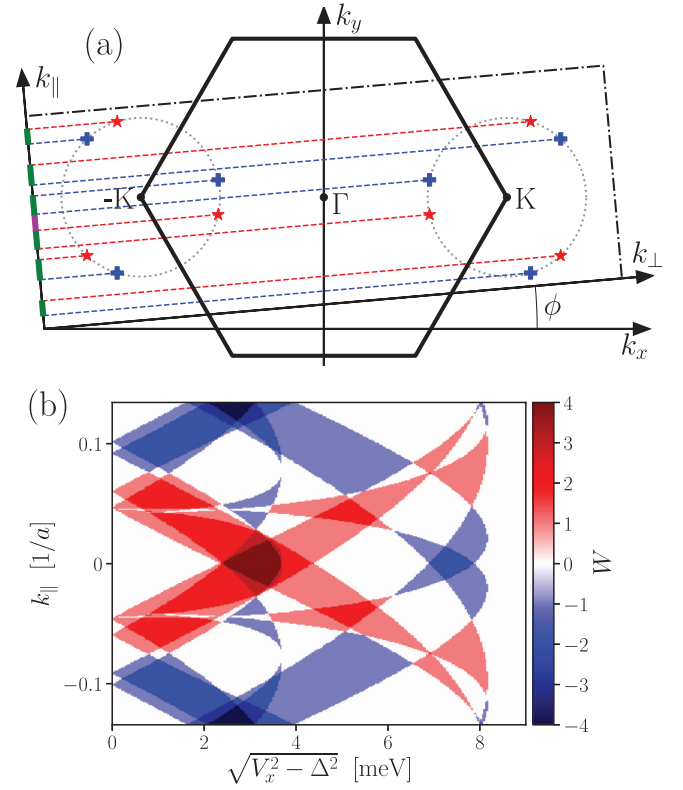edge projections of the nodal points are connected by flat bands of zero-energy Andreev edge states. These flat bands are protected by chiral symmetry. Our conclusions are based on a study of both continuum and atomic tight-binding models.

Finally, we address experimental feasibility. It is possible to produce high-quality monolayer MoX$_2$ crystals with low impurity densities and sizes in the tens of microns or even millimeters [62–65]. Such large samples may guarantee that the topological Andreev edge states at opposing edges are well separated. In addition, recent experiments show that thin films even down to monolayers of MoX$_2$ become superconducting in the conduction band at carrier densities $\gtrsim 6 \times 10^{13}$ cm^{-2} [26,28,29], which translates to a minimum chemical potential μ_0 for superconductivity of 153 meV (MoS$_2$), 120 meV (MoSe$_2$), and 117 meV (MoTe$_2$). The mismatch of μ_0 and $\mu_{1,2}$ in MoS$_2$ implies that intrinsic superconductivity is not suitable to realize the nodal topological phase in MoS$_2$, but this can potentially be overcome using the proximity effect. In addition, a recent experiment indicates possible intrinsic

TABLE I. Chemical potentials $\mu_{1,2}$ in meV for MoS_2, $MoSe_2$, and $MoTe_2$ [see also Fig. 1(b)], obtained from the continuum model.

	MoS_2	$MoSe_2$	$MoTe_2$
μ_1	32.6	126.7	136.1
μ_2	34.5	143.0	184.5

unconventional pairing in MoS_2 at very large doping [66]. For monolayer $MoSe_2$ and $MoTe_2$, μ_0 is close to $\mu_{1,2}$ in Fig. 1(b) [see Table I], and therefore these two materials are promising candidates for realizing nodal TSCs. For experimental detection, aside from tunneling measurements, the character of bulk nodal points could be probed using quasiparticle interference or local pair-breaking measurements [15,16,67]. Because the flat bands manifest as a zero-energy density of states peak in the nontrivial parts of the phase diagram Fig. 1(b), it is possible to discern them from other edge states [68], which generally don't stick to zero energy, by tuning the magnetic field and/or chemical potential. If the chiral symmetry is broken, the flat bands may split from zero energy. Two possible causes are a perpendicular electric field due to asymmetric electrostatic gating and an out-of-plane Zeeman field. The electric field can be avoided by chemical doping [26,28] and it is possible to align the magnetic field along the in-plane direction to a precision of $\lesssim 0.02°$, such that the out-of-plane projection is negligible [30].

[1] J. Alicea, Rep. Prog. Phys. **75**, 076501 (2012).

[2] M. Leijnse and K. Flensberg, Semicond. Sci. Technol. **27**, 124003 (2012).

[3] C. Beenakker, Annu. Rev. Condens. Matter Phys. **4**, 113 (2013).

[4] A. Y. Kitaev, Phys. Usp. **44**, 131 (2001).

[5] S. B. Bravyi and A. Y. Kitaev, Ann. Phys. **298**, 210 (2002).

[6] C. Nayak, S. H. Simon, A. Stern, M. Freedman, and S. Das Sarma, Rev. Mod. Phys. **80**, 1083 (2008).

[7] S. Kashiwaya and Y. Tanaka, Rep. Prog. Phys. **63**, 1641 (2000).

[8] T. Löfwander, V. S. Shumeiko, and G. Wendin, Supercond. Sci. Technol. **14**, R53 (2001).

[9] A. P. Schnyder and P. M. R. Brydon, J. Phys.: Condens. Matter **27**, 243201 (2015).

[10] S. Ryu and Y. Hatsugai, Phys. Rev. Lett. **89**, 077002 (2002).

[11] M. Sato, Y. Tanaka, K. Yada, and T. Yokoyama, Phys. Rev. B **83**, 224511 (2011).

[12] A. P. Schnyder, P. M. R. Brydon, and C. Timm, Phys. Rev. B **85**, 024522 (2012).

[13] C. C. Tsuei and J. R. Kirtley, Rev. Mod. Phys. **72**, 969 (2000).

[14] Y. Kasahara, T. Iwasawa, H. Shishido, T. Shibauchi, K. Behnia, Y. Haga, T. D. Matsuda, Y. Onuki, M. Sigrist, and Y. Matsuda, Phys. Rev. Lett. **99**, 116402 (2007).

[15] B. B. Zhou, S. Misra, E. H. da Silva Neto, P. Aynajian, R. E. Baumbach, J. D. Thompson, E. D. Bauer, and A. Yazdani, Nat. Phys. **9**, 474 (2013).

[16] M. P. Allan, F. Massee, D. K. Morr, J. Van Dyke, A. W. Rost, A. P. Mackenzie, C. Petrovic, and J. C. Davis, Nat. Phys. **9**, 468 (2013).

[17] K. Yada, M. Sato, Y. Tanaka, and T. Yokoyama, Phys. Rev. B **83**, 064505 (2011).

[18] A. P. Schnyder and S. Ryu, Phys. Rev. B **84**, 060504 (2011).

[19] M. H. Fischer, T. Neupert, C. Platt, A. P. Schnyder, W. Hanke, J. Goryo, R. Thomale, and M. Sigrist, Phys. Rev. B **89**, 020509 (2014).

[20] T. Meng and L. Balents, Phys. Rev. B **86**, 054504 (2012).

[21] C. L. M. Wong, J. Liu, K. T. Law, and P. A. Lee, Phys. Rev. B **88**, 060504 (2013).

[22] B. Huang, X. Yang, N. Xu, and M. Gong, Phys. Rev. B **97**, 045142 (2018).

[23] L. Fu and C. L. Kane, Phys. Rev. Lett. **100**, 096407 (2008).

[24] J. D. Sau, R. M. Lutchyn, S. Tewari, and S. Das Sarma, Phys. Rev. Lett. **104**, 040502 (2010).

[25] Q. H. Wang, K. Kalantar-Zadeh, A. Kis, J. N. Coleman, and M. S. Strano, Nat. Nanotech. **7**, 699 (2012).

[26] J. T. Ye, Y. J. Zhang, R. Akashi, M. S. Bahramy, R. Arita, and Y. Iwasa, Science **338**, 1193 (2012).

[27] K. Taniguchi, A. Matsumoto, H. Shimotani, and H. Takagi, Appl. Phys. Lett. **101**, 042603 (2012).

[28] J. M. Lu, O. Zheliuk, I. Leermakers, N. F. Q. Yuan, U. Zeitler, K. T. Law, and J. T. Ye, Science **350**, 1353 (2015).

[29] W. Shi, J. Ye, Y. Zhang, R. Suzuki, M. Yoshida, J. Miyazaki, N. Inoue, Y. Saito, and Y. Iwasa, Sci. Rep. **5**, 12534 (2015).

[30] Y. Saito, Y. Nakamura, M. S. Bahramy, Y. Kohama, J. Ye, Y. Kasahara, Y. Nakagawa, M. Onga, M. Tokunaga, T. Nojima, Y. Yanase, and Y. Iwasa, Nat. Phys. **12**, 144 (2016).

[31] D. Costanzo, S. Jo, H. Berger, and A. F. Morpurgo, Nat. Nanotech. **11**, 339 (2016).

[32] X. Xi, Z. Wang, W. Zhao, J.-H. Park, K. T. Law, H. Berger, L. Forró, J. Shan, and K. F. Mak, Nat. Phys. **12**, 139 (2016).

[33] O. Zheliuk, J. Lu, J. Yang, and J. Ye, Phys. Status Solidi RRL **11**, 1700245 (2017).

[34] S. C. de la Barrera, M. R. Sinko, D. P. Gopalan, N. Sivadas, K. L. Seyler, K. Watanabe, T. Taniguchi, A. W. Tsen, X. Xu, D. Xiao, and B. M. Hunt, Nat. Commun. **9**, 1427 (2018).

[35] B. T. Zhou, N. F. Q. Yuan, H.-L. Jiang, and K. T. Law, Phys. Rev. B **93**, 180501 (2016).

[36] S. Ilić, J. S. Meyer, and M. Houzet, Phys. Rev. Lett. **119**, 117001 (2017).

[37] Z. Y. Zhu, Y. C. Cheng, and U. Schwingenschlögl, Phys. Rev. B **84**, 153402 (2011).

[38] D. Xiao, G.-B. Liu, W. Feng, X. Xu, and W. Yao, Phys. Rev. Lett. **108**, 196802 (2012).

[39] W.-Y. He, B. T. Zhou, J. J. He, N. F. Q. Yuan, T. Zhang, and K. T. Law, Commun. Phys. **1**, 40 (2018).

[40] R. Roldán, M. P. López-Sancho, F. Guinea, E. Cappelluti, J. A. Silva-Guillén, and P. Ordejón, 2D Mater. **1**, 034003 (2014).

[41] C. L. Kane and E. J. Mele, Phys. Rev. Lett. **95**, 226801 (2005).

[42] J. C. Slater and G. F. Koster, Phys. Rev. **94**, 1498 (1954).

[43] R. Peierls, Z. Phys. **80**, 763 (1933).

[44] D. R. Hofstadter, Phys. Rev. B **14**, 2239 (1976).

[45] T. B. Boykin, R. C. Bowen, and G. Klimeck, Phys. Rev. B **63**, 245314 (2001).

[46] S. Fang, R. Kuate Defo, S. N. Shirodkar, S. Lieu, G. A. Tritsaris, and E. Kaxiras, Phys. Rev. B **92**, 205108 (2015).

[47] P. Löwdin, J. Chem. Phys. **19**, 1396 (1951).

[48] L. Wang and M. W. Wu, Phys. Rev. B **89**, 115302 (2014).

[49] See Supplemental Material at http://link.aps.org/supplemental/10.1103/PhysRevB.98.205411 for further details, which includes the additional Refs. [40–45].

[50] A. P. Schnyder, S. Ryu, A. Furusaki, and A. W. W. Ludwig, Phys. Rev. B **78**, 195125 (2008).

[51] C.-K. Chiu, J. C. Teo, A. P. Schnyder, and S. Ryu, Rev. Mod. Phys. **88**, 035005 (2016).

[52] D. Varjas, T. Ö. Rosdahl, and A. R. Akhmerov, New J. Phys. **20**, 093026 (2018).

[53] The 1D PHS or TRS that only flip $k_\perp$ require an extra unitary symmetry that maps $k_\parallel \to -k_\parallel$, but we find that no such symmetry exists for generic $(k_\perp, k_\parallel)$.

[54] For the armchair direction $k_\parallel = k_y \hat{y}$, although the 1D Hamiltonian of the continuum model belongs to class BDI, it turns out to be in class AIII in the tight-binding models, due to the absence of a point group symmetry that maps $y \to -y$.

[55] B. Béri, Phys. Rev. B **81**, 134515 (2010).

[56] G.-B. Liu, W.-Y. Shan, Y. Yao, W. Yao, and D. Xiao, Phys. Rev. B **88**, 085433 (2013).

[57] K. Kośmider, J. W. González, and J. Fernández-Rossier, Phys. Rev. B **88**, 245436 (2013).

[58] A. Kormányos, G. Burkard, M. Gmitra, J. Fabian, V. Zólyomi, N. D. Drummond, and V. Fal'ko, 2D Mater. **2**, 022001 (2015).

[59] S. Datta, *Electronic Transport in Mesoscopic Systems*, Cambridge Studies in Semiconductor Physics and Microelectronic Engineering (Cambridge University Press, Cambridge, 1995).

[60] C. W. Groth, M. Wimmer, A. R. Akhmerov, and X. Waintal, New J. Phys. **16**, 063065 (2014).

[61] P. Delplace, D. Ullmo, and G. Montambaux, Phys. Rev. B **84**, 195452 (2011).

[62] J. N. Coleman, M. Lotya, A. O'Neill, S. D. Bergin, P. J. King, U. Khan, K. Young, A. Gaucher, S. De, R. J. Smith, I. V. Shvets, S. K. Arora, G. Stanton, H.-Y. Kim, K. Lee, G. T. Kim, G. S. Duesberg, T. Hallam, J. J. Boland, J. J. Wang, J. F. Donegan, J. C. Grunlan, G. Moriarty, A. Shmeliov, R. J. Nicholls, J. M. Perkins, E. M. Grieveson, K. Theuwissen, D. W. McComb, P. D. Nellist, and V. Nicolosi, Science **331**, 568 (2011).

[63] M. Chhowalla, H. S. Shin, G. Eda, L.-J. Li, K. P. Loh, and H. Zhang, Nat. Chem. **5**, 263 (2013).

[64] X. Wang, Y. Gong, G. Shi, W. L. Chow, K. Keyshar, G. Ye, R. Vajtai, J. Lou, Z. Liu, E. Ringe, B. K. Tay, and P. M. Ajayan, ACS Nano **8**, 5125 (2014).

[65] J. Chen, X. Zhao, S. J. R. Tan, H. Xu, B. Wu, B. Liu, D. Fu, W. Fu, D. Geng, Y. Liu, W. Liu, W. Tang, L. Li, W. Zhou, T. C. Sum, and K. P. Loh, J. Am. Chem. Soc. **139**, 1073 (2017).

[66] D. Costanzo, H. Zhang, B. A. Reddy, H. Berger, and A. F. Morpurgo, Nat. Nanotechnol. **13**, 483 (2018).

[67] T. Hanaguri, Y. Kohsaka, J. C. Davis, C. Lupien, I. Yamada, M. Azuma, M. Takano, K. Ohishi, M. Ono, and H. Takagi, Nat. Phys. **3**, 865 (2007).

[68] H. Rostami, R. Asgari, and F. Guinea, J. Phys.: Condens. Matter **28**, 495001 (2016).